Nanoscale

PAPER

View Article Online
View Journal

Cite this: DOI: 10.1039/d6nr00012f

Ultrafast charge dynamics of diketopyrrolopyrrole-based terpolymers for optoelectronic applications: impact of acceptor concentrations and thermal annealing

Leonato Tambua Nchinda, *[a] Zewdneh Genene, [b] Wendimagegn Mammo, [c] Newayemedhin A. Tegegne, [d] Dirk M. Guldi [e] and Tjaart P. J. Krüger *[a]

Diketopyrrolopyrrole (DPP)-based terpolymers have emerged as promising donor materials for organic solar cells (OSCs), offering tunable optoelectronic properties, broadband absorption, and enhanced morphological stability through random terpolymerization strategies. This study investigates the ultrafast charge carrier dynamics of three DPP-based terpolymers, (**P1–P3**), incorporating different ratios of fluorobenzotriazole (FTAZ) and thienothiophene-capped DPP (TTDPP) acceptors. Using femtosecond transient absorption spectroscopy, we examine how acceptor ratios and thermal annealing influence photophysical processes in pristine terpolymers and their bulk heterojunction blends with $PC_{71}BM$. Increasing the TTDPP content enhances backbone planarity, π–π stacking, and charge delocalization, thereby reducing recombination losses and promoting efficient charge separation. Compared to **P2** and **P3**, the **P1** terpolymer, with the highest TTDPP ratio, exhibits the most favorable intramolecular charge transfer kinetics and balanced carrier mobilities, consistent with its superior photovoltaic performance. Thermal annealing, however, reduces long-lived charge populations in all blends due to fullerene aggregation, which diminishes phase separation. These findings highlight how rational tuning of acceptor ratios in DPP-based terpolymers provides a pathway toward optimizing both efficiency and stability in OSCs.

Received 1st January 2026,
Accepted 27th March 2026

DOI: 10.1039/d6nr00012f

rsc.li/nanoscale

1. Introduction

Organic solar cells (OSCs) offer a compelling renewable energy option due to their cost-effectiveness, lightweight, flexibility, and semi-transparency.[1] Over the last two decades, substantial advancements, especially in the development of non-fullerene acceptors, have played a pivotal role in enhancing the power conversion efficiency (PCE) in OSCs beyond 20%.[2–8] These devices commonly employ a bulk heterojunction (BHJ) structure, in which a blend of electron donor (D) and acceptor (A) materials forms an interconnected nanoscale network that facilitates efficient charge separation and movement. The polymer donors remain vital in OSCs as they provide a balanced phase separation and domain crystallinity within the polymer D : A bulk heterojunction (BHJ), crucial for efficient charge generation and collection, thus enabling high PCEs.[9–11] However, achieving commercial viability in OSCs requires not only high efficiency but also extended stability under typical OSC conditions, such as sustained light exposure, heat, and temperature fluctuations from day to night.[12–16]

Random terpolymerization has emerged as a promising approach to enhance the photovoltaic performance and stability of polymer donors.[11,17–19] This method involves adding a second donor or acceptor unit, transforming the polymer from a D–A type copolymer to configurations like D_1–A–D_2–A or D–A_1–D–A_2 terpolymers.[11,20–22] The second donor (or acceptor) moiety affects the polymer's optical absorption, energy levels, and blend morphology.[20] For instance, Yang *et al.* showed that introducing just 5% of the donor moiety thieno[3,2-*b*]thiophene (TT) into poly[[4,8-bis[5-(2-ethylhexyl)-2-thienyl]benzo[2-*b*:4,5-*b*′]dithiophene-2,6-diyl]-2,5-thiophenediyl[5,7-bis(2-ethylhexyl)-4,8-dioxo-4*H*,8*H*-benzo[2-*c*:4,5-*c*′]dithiophene-1,3-diyl]] (PBDB-T) improved the absorption coefficient and optimized

[a]*Department of Physics, University of Pretoria, Private Bag X20, Hatfield, 0028, South Africa. E-mail: leonato.nchinda@tuks.co.za, tjaart.kruger@up.ac.za*
[b]*Department of Chemistry and Chemical Engineering, Chalmers University of Technology, SE412 96 Gothenburg, Sweden*
[c]*Department of Chemistry, Addis Ababa University, 33658 Addis Ababa, Ethiopia*
[d]*Department of Physics, Addis Ababa University, Addis Ababa, 1176, Ethiopia*
[e]*Department of Chemistry and Pharmacy & Interdisciplinary Center for Molecular Materials (ICMM), FAU Profile Center Solar, Friedrich-Alexander-Universität Erlangen-Nürnberg, Erlangen, Germany*

film morphology, resulting in higher PCEs in terpolymer donor devices based on $PC_{71}BM$ and m-ITIC.[23]

Beyond enhancing PCE, random terpolymerization also shows promise for improving OSC stability. For example, we developed and synthesized three diketopyrrolopyrrole (DPP)-based donor terpolymer materials (**P1–P3**) with configuration D–A_1–D–A_2, which differed in the ratio of the two acceptors (FTAZ and TTDPP) in the backbone (thienyl-substituted benzodithiophene, BDTT) of the terpolymers.[11] The FTAZ : TTDPP ratios were 1 : 3, 1 : 1, and 3 : 1 for **P1**, **P2**, and **P3**, respectively. The highest PCEs of these terpolymers were 5.6% in $PC_{71}BM$-based devices and 6.3% in IECO-4F-based devices, with the latter representing one of the best efficiencies for fullerene-free polymer solar cells incorporating DPP-based polymers. This high performance obtained by tuning the ratio of TTDPP and FTAZ was due to the broadening of the absorption spectrum of the terpolymers, which extended between 300 and 900 nm. We observed that the absorption of the terpolymers could be effectively broadened by increasing the TTDPP concentration in their backbone (**P3** < **P2** < **P1**), while stronger absorption in the region between 450 and 600 nm could be achieved with a higher FTAZ ratio (**P1** < **P2** < **P3**) due to its lower electron-accepting nature.[18] This confirms that rational coupling of the moieties in the terpolymers could be an effective route to enhance the photocurrent in the resultant OSCs.[11,19]

The promising PCE observed in the terpolymers (Table S1 of the SI) led us to further explore the thermal stability of the terpolymers and their blends with $PC_{71}BM$.[15] After thermal annealing at 85 °C for 3 and 24 h, we observed that thermal degradation had no sizeable effect on the molecular properties of the terpolymers. We also noticed that incorporation of the FTAZ acceptor served as a viable route in enhancing the thermal stability of the BHJ active layers. This suggests that random terpolymerization could be a viable approach to achieving more stable and efficient OSCs.

While the terpolymers remained structurally stable under thermal stress, the blend morphology exhibited time-dependent evolution, as reported previously.[15] Specifically, upon thermal annealing, the terpolymers underwent inter- and intrachain molecular rearrangement without phase segregation. However, in the terpolymer : $PC_{71}BM$ blends, thermal annealing induced pronounced morphological evolution, wherein $PC_{71}BM$ molecules progressively dissociated from the terpolymer matrix and formed distinct aggregates, as evidenced by the AFM and TEM images (Fig. S1 and S2, respectively, of the SI). This aggregation disrupts the initially homogeneous **P1–P3** : $PC_{71}BM$ BHJ morphology by promoting phase separation of $PC_{71}BM$ from the terpolymer matrix, resulting in the formation of larger fullerene-rich domains. As these domains grow beyond the exciton diffusion length of the active layer, exciton dissociation becomes less efficient, thereby limiting the generation and transport of free charge carriers to the electrodes and ultimately reducing the photocurrent.[24,25] Therefore, upon thermal annealing, the $PC_{71}BM$ molecules progressively diffused out of the terpolymer matrix and formed sizable aggregates at the sample–air interface, consistent with increased surface roughness as determined from the AFM images (Fig. S1 of the SI). The reduced interfacial area may result in a decrease in short-circuit current density, while increased surface roughness may compromise electrode contact, negatively affecting the fill factor.[24] Importantly, despite these morphological changes, no clear molecular or chemical degradation of the **P1–P3** : $PC_{71}BM$ active layers was observed, which is a unique characteristic required for the development of more efficient and stable BHJ OSCs, where efficient charge separation and long-term device stability rely sensitively on nanoscale donor–acceptor organization. Nevertheless, there are still a limited number of studies examining the relationship between free charge carrier dynamics and morphology in DPP-based terpolymer OSCs. This limits our understanding of specific design principles that ensure both improved PCE and stability, as well as the mechanisms behind these enhancements.

Here, we investigated the photophysics of **P1**, **P2**, and **P3** as pristine terpolymer films and blends with $PC_{71}BM$ using steady-state absorption and ultrafast transient absorption (TA) spectroscopy. The results reveal that **P1** achieves faster intramolecular charge transfer (ICT), in line with more balanced electron and hole mobility when combined with $PC_{71}BM$ as reported in our previous study.[11] This charge delocalization decreases coulombic attraction, facilitates the separation of charge transfer states, and minimizes voltage loss. Hence, the different acceptor ratios in the terpolymer backbone have a substantial impact on key performance parameters and the PCE of OSCs.

2. Experimental methods

The molecular structures of the random terpolymers **P1–P3** are presented in Scheme 1.[11] The synthesis scheme of the terpolymers, including their molecular weight, structural characterization, and optimization, has been reported in our previous publication.[11] These terpolymers adopt a D–A_1–D–A_2 configuration, in which thienyl-substituted benzodithiophene (BDTT) functions as the electron-donating (D) unit, while fluorobenzotriazole (FTAZ, A1) and thienothiophene-capped diketopyrrolopyrrole (TTDPP, A2) act as the electron-accepting moieties. Varying the relative amounts of FTAZ and TTDPP enables systematic tuning of the optical absorption and energy levels of the resulting terpolymers.[11] To investigate how these acceptor ratios influence the optoelectronic and photophysical properties of prospective OSC active layers, three compositions–FTAZ : TTDPP ratios of 1 : 3, 1 : 1, and 3 : 1 corresponding to **P1**, **P2**, and **P3**, respectively–were employed, as shown in Scheme 1. Regioregular [6,6]-phenyl-C_{71}-butyric acid methyl ester ($PC_{71}BM$) was purchased from Ossila and used without further purification. Glass substrates were used for thin film fabrication, and 1,2-dichlorobenzene (DCB), obtained from Sigma-Aldrich, was used as received.

Thin films of the pristine terpolymers and the corresponding **P1–P3** : $PC_{71}BM$ bulk heterojunction (BHJ) blends

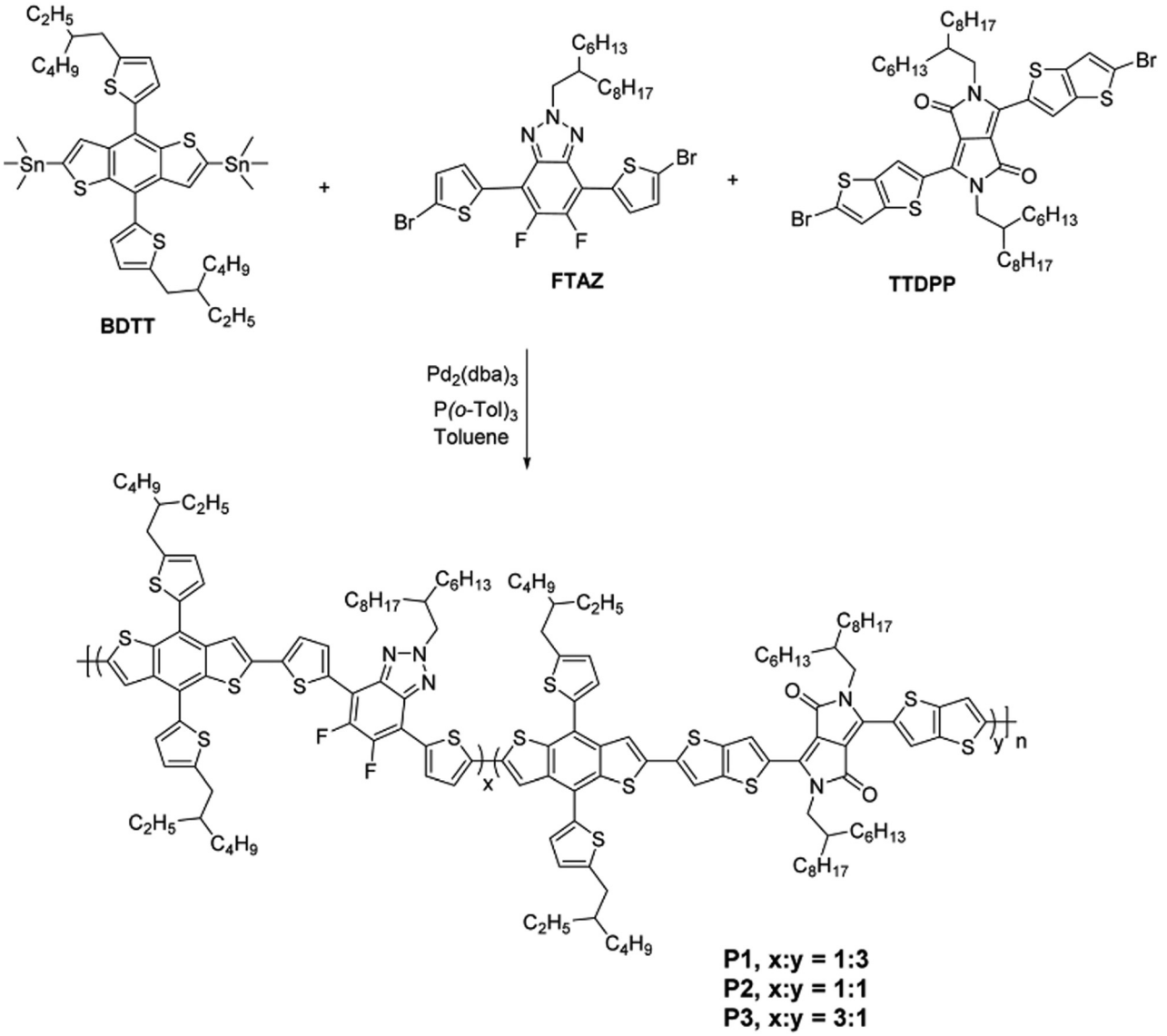

Scheme 1 Molecular structure of the terpolymers **P1–P3**, highlighting their structural building blocks.

were prepared following the procedure outlined below. Glass substrates were cleaned in an ultrasonic bath using a soap solution, deionised water, acetone, and isopropanol for 10 minutes each, after which they were dried with nitrogen. The active layers–comprising each terpolymer blended with $PC_{71}BM$ in DCB–were then spin-coated onto the substrates at 1200 rpm for 60 seconds. The blend solutions were prepared at a **P1–P3** : $PC_{71}BM$ ratio of 1 : 1.5 with a total concentration of 25 mg mL^{-1} in DCB and were stirred at 50 °C for 3 hours to ensure complete dissolution. To induce thermal degradation, the thin films were thermally annealed at 85 °C for 24 hours.

The absorption spectra of the pristine terpolymers in DCB solution and thin film were recorded using a PerkinElmer Lambda 19 ultraviolet-visible-near infrared (UV-VIS-NIR) spectrophotometer. All spectra were acquired at room temperature. Femtosecond TA spectroscopy was conducted using an Astrella-F-1K amplified Ti:sapphire femtosecond laser system from Coherent, operating at a repetition rate of 1 kHz, 5.5 W power (5.5 mJ pulse energy), and a pulse duration of 80 fs, with a TA pump/probe Helios detection system from Ultrafast Systems. White light was generated by focusing a fraction of the fundamental 800 nm output onto a 2 mm CaF_2 mounted on a translating crystal holder. A 1.2 mJ fraction of the fundamental was used for pump beam generation by a TOPAS Prime from Light Conversion with standard NIRUVIS extension. An optical delay line allowed for time delays up to 7.3 ns. A depolarizer was placed in the pump beam to avoid rotational dynamics. Bandpass filters with ±5 or ±10 nm were used to ensure low spectral width and to exclude 800 nm photons. The VIS and NIR TA spectra were measured separately. By selecting wavelengths corresponding to specific absorption features, kinetic traces were extracted. These traces were then fitted using a multiexponential function to facilitate multi-wavelength analysis and understanding of the dynamics observed.

3. Results and discussion

3.1. Steady-state spectroscopy

The steady-state absorption and emission spectra of the pristine terpolymers in thin film and solution are presented in Fig. 1(a)–(c). The absorption spectra of the pristine terpolymer films display three main bands, with the first band between 350 and 450 nm attributed to terpolymer backbone π–π* transitions and intramolecular charge transfer (ICT) from the donor, BDTT, to the two acceptors, FTAZ and TTDPP, as shown in Fig. 1(a–c). This multiband profile is a common feature of alternating co-/terpolymers.[26] All terpolymers also demonstrated broad absorption in DCB solution, with central absorption peaks (A_{0-0}) occurring at approximately 748 nm for **P1**, 737 nm for **P2**, and 733 nm for **P3** (see Fig. 1(a–c)). The increased absorption of **P1** in the NIR is attributed to a higher ratio of the TTDPP acceptor, which improves the conjugation length and planarity of the **P1** terpolymer backbone, enhances π–π conjugation, and facilitates efficient ICT.[27–29]

Upon 600 nm photoexcitation in DCB solution, all three terpolymers, **P1–P3** exhibited multiple fluorescence bands. Comparison of the absorption and emission spectra indicates that the emission arises from two distinct ICT states: from the donor, BDTT, to the two acceptors, FTAZ and TTDPP. This indicates that in the terpolymers, two ICT states are established at the different D–A interfaces. The emission profile can thus be divided into regions below and above 720 nm: the lower-energy part can be associated with the BDTT to TTDPP ICT transition, while the higher-energy part can be associated with the BDTT to FTAZ ICT transition. The pristine films also exhibited broad absorption, with central peaks at around 761, 746, and 739 nm for **P1**, **P2**, and **P3**, respectively, as indicated in Fig. 1(a–c). Compared to their solution states, the pristine **P1** film displayed a redshift of about 13 nm, while **P2**- and **P3**-based films exhibited smaller red shifts of approximately 9 and 6 nm, respectively. This notable redshift in the pristine **P1** film suggests stronger intermolecular interactions, resulting in a more organized molecular orientation and denser molecular stacking.[30–32]

We used $PC_{71}BM$ as the acceptor polymer to explore the differences in the photophysical processes among the three donor materials within the BHJ (Fig. 1(d)). Compared to the blend films of **P2** and **P3**, the **P1** blend exhibited a greater solar utilization efficiency, leading to a wider photo-to-current response range and higher short-circuit current density (J_{sc}) as reported in our previous study[11] (see Table S1 of the SI) The weak non-covalent intermolecular interactions present in **P3** restricted the charge delocalization hopping distance, thereby increasing the likelihood of charge recombination. Conversely, **P1** displayed a pronounced absorption peak (A_{0-0}), indicative of strong π–π stacking and a higher density of molecular states. The increased ratio of the TTDPP acceptor allowed **P1** to adopt a planar molecular backbone, which improved non-covalent intermolecular interactions, extended π-conjugation

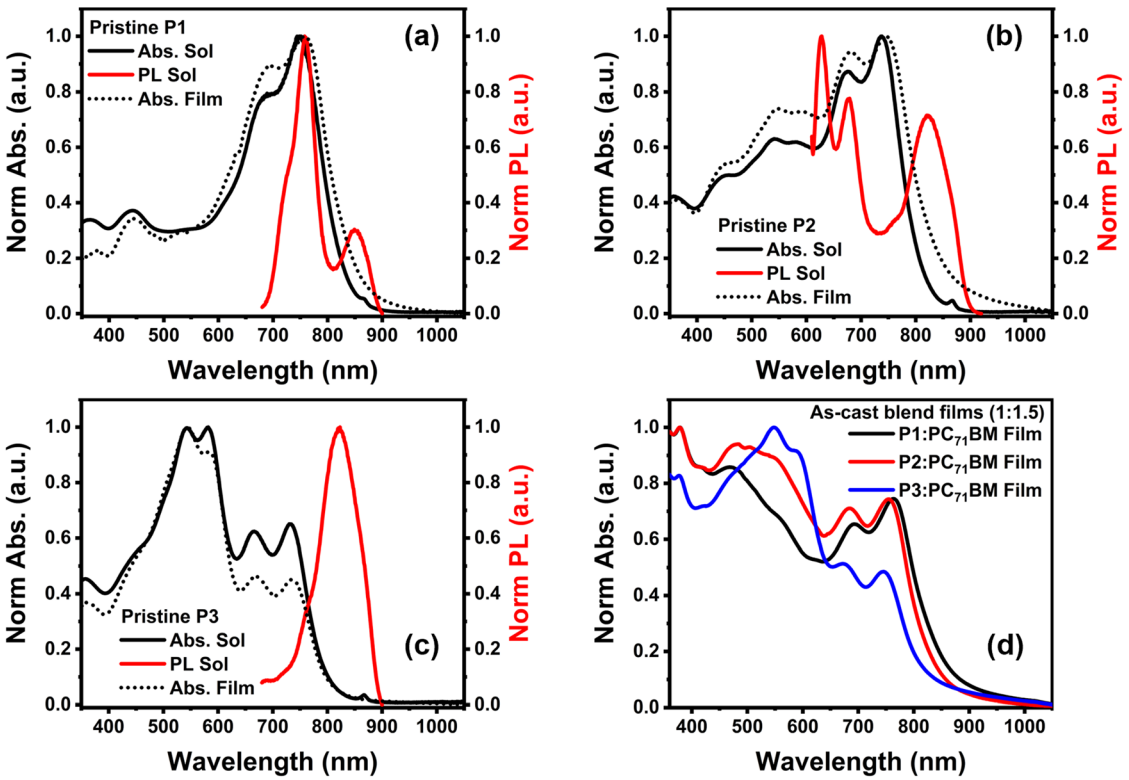

Fig. 1 Absorption (a–d) and photoluminescence (a–c) spectra of (a–c) pristine terpolymers in solution and film and (d) terpolymer : $PC_{71}BM$ thin films.

and minimized overaggregation, as reflected in the lower RMS roughness of the **P1** blend films.[15] The robust non-covalent interactions and high density of molecular states in three-dimensional (3D) regular orientations contribute to greater stability and promote longer-range charge delocalization, thereby reducing delocalization energy and limiting charge recombination. Importantly, the extended charge delocalization facilitates the reduction of the energy barrier for separating interfacial charge transfer (CT) states into free charges, effectively decreasing energy loss.[33]

3.2. Transient absorption spectroscopy of pristine terpolymers

The influence of varying acceptor concentrations on ultrafast charge dynamics was investigated using TA spectroscopy. Fig. 2 and Fig. S3 of the SI show the TA spectra for pristine **P1**, **P2**, and **P3** thin films excited at 600 nm. The spectra of all three terpolymers reveal a broad negative differential absorption band from around 450 nm to about 750 nm. This negative band is attributed to ground state bleaching (GSB) arising from the depletion of the ground state, as this wavelength range aligns closely with the steady-state absorption profiles of the terpolymers. Specifically, the negative signal observed near 600 nm corresponds to GSB and stimulated emission (SE) from the local excited (LE) state of the molecule following photoexcitation. In the initial stages (within the first 5 ps), the negative signal around 600 nm decreases over time, while the negative signal near 740 nm and the positive signal at 1140 nm both increase (see Fig. S3 of the SI). These transient spectral variations are characteristic indicators of ICT.[28,29,34,35] Therefore, the negative signal peaking at 740 nm can be linked to the stimulated emission of the intermolecular charge transfer (ICT) state while the positive signal at around 1140 nm can be associated with excited state absorption (ESA) from either the direct LE or ICT state. At longer time delays (7 ns), nearly no ESA signal was detected in any of the terpolymers, indicating that recombination in excited states occurs within a few hundred picoseconds. Therefore, triplet states can be ruled out as the primary source of this ESA due to their rapid decay characteristics.

Despite these common spectral features, clear differences emerge among the terpolymers. In **P1**, the ICT-related features show a relatively strong and rapid kinetics, suggesting more efficient exciton-to-ICT conversion (within 1.3 ps) compared to

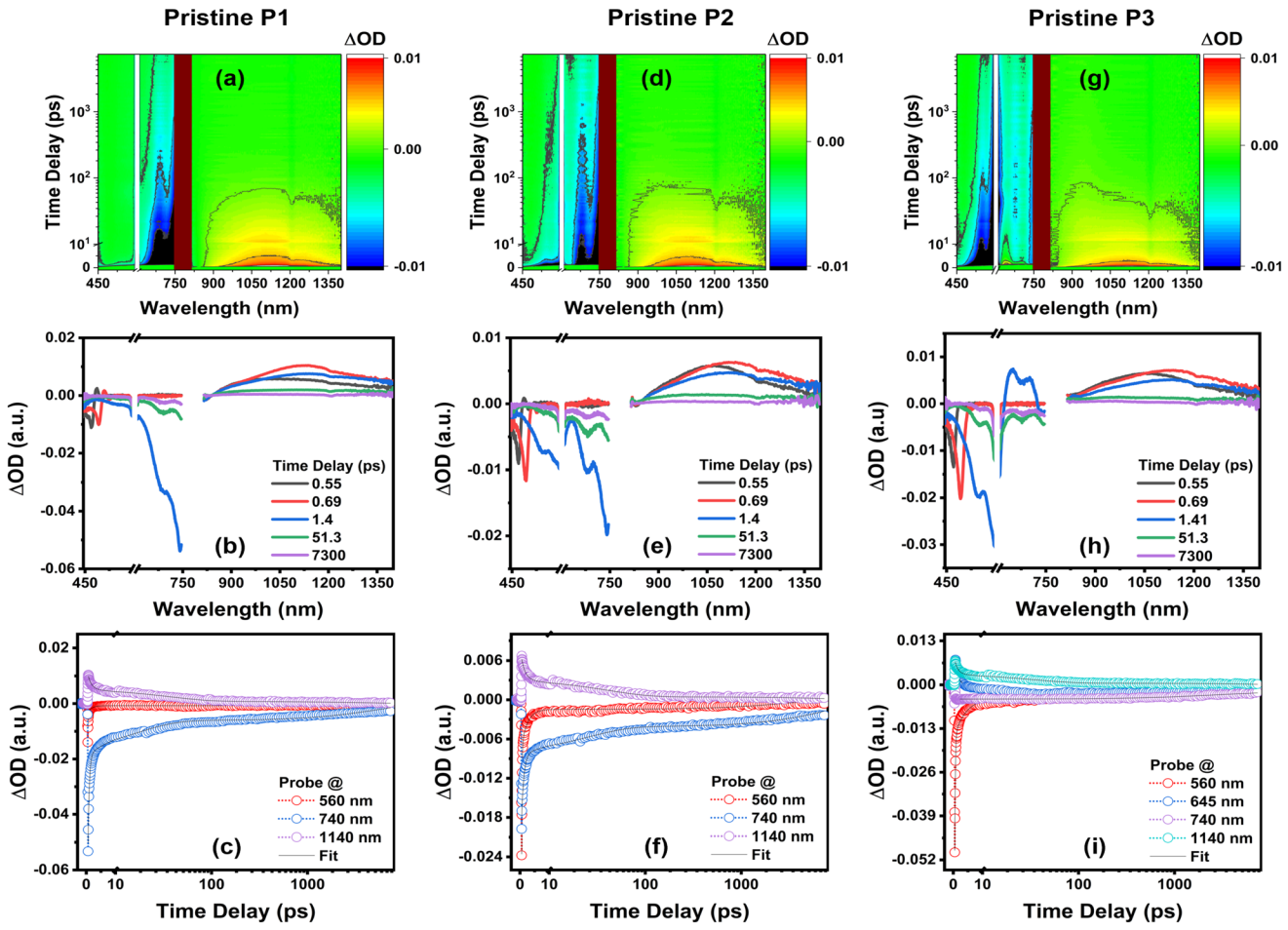

Fig. 2 TA spectra of as-cast pristine (a and b) **P1** (d and e) **P2**, and (g and h) **P3** thin films excited at 600 nm at 0.5 μJ per pulse per cm^2. TA traces probed at different wavelengths from the pristine (c) **P1** (f) **P2** and (i) **P3** films pumped at 600 nm.

P2 (2.1 ps) and **P3** (3.9 ps). In contrast, the **P2** film shows similar spectral signatures but with weaker ICT formation and slower dynamics, indicating reduced efficiency of charge transfer pathways in this composition. The **P3** film exhibits an additional ESA feature around 650 nm, which is absent in **P1** and **P2**. The presence of this extra ESA highlights a stronger competition between LE relaxation and ICT formation in **P3**, further limiting its ICT efficiency.

To gain deeper insight into how excitation energy influences these differences, we next examined the TA response under low-energy photon excitation. Fig. 3 and Fig. S4 of the SI illustrate that low-energy photons primarily excite the ICT band of the pristine terpolymers. As a result, the transient spectrum rapidly displays the GSB signal of the ICT state, with the LE state showing negligible GSB, particularly in the pristine **P1** terpolymer. Among the three terpolymers, a more rapid ICT process was noted with the highest content of TTDPP in **P1** (see Fig. 3(c)), while the material with the highest FTAZ ratio, **P3**, exhibited a slower ICT process due to its weaker electron-accepting properties (see Fig. 3(i)).

Therefore, in Fig. 2, it is observed that under high-energy photoexcitation, the excited state of **P1** (see Fig. 2(c)) transitions to the ICT state more rapidly than that of **P2** (see Fig. 2(f)) and **P3** (see Fig. 2(i)). It is noteworthy that no spectral distortion occurs over longer time delays, further indicating that the initial spectral changes are intermolecular in nature. Fig. 2(c) illustrates the kinetic results for pristine **P1** film following high-energy excitation, where a decrease in the signal at 560 nm coincides with an increase at 740 and 1140 nm with a lifetime of about 1.3 ps. Fig. 2(f and i) present the results for **P2** and **P3** under high-energy excitation, demonstrating a continued slow ICT process with a lifetime of 2.1 ps and 3.9 ps in **P2** and **P3** respectively. Fig. 3(c, f, and i) depict the kinetics results under low-energy excitation, where the ICT is directly excited by low-energy photons, leading to a rapid generation of the signal in **P1**, which then decays without a transfer process. In summary, while all three terpolymers display characteristic LE and ICT features with ultrafast recombination dynamics, **P1** demonstrates the most efficient ICT formation, **P2** exhibits weaker ICT population, and **P3** shows competing LE pathways alongside ICT. These findings underscore how variations in acceptor concentration within the terpolymer backbone strongly modulate ultrafast charge-carrier dynamics.

To further contextualize these film-based results, we examined the ultrafast charge dynamics of the pristine terpolymers in solution. We therefore investigated the ultrafast charge dynamics of pristine terpolymers dissolved in DCB solution using 600 nm excitation, with the findings presented in Fig. S5 and S6 of the SI. This comparison between solution and film measurements provides a baseline to disentangle intrinsic

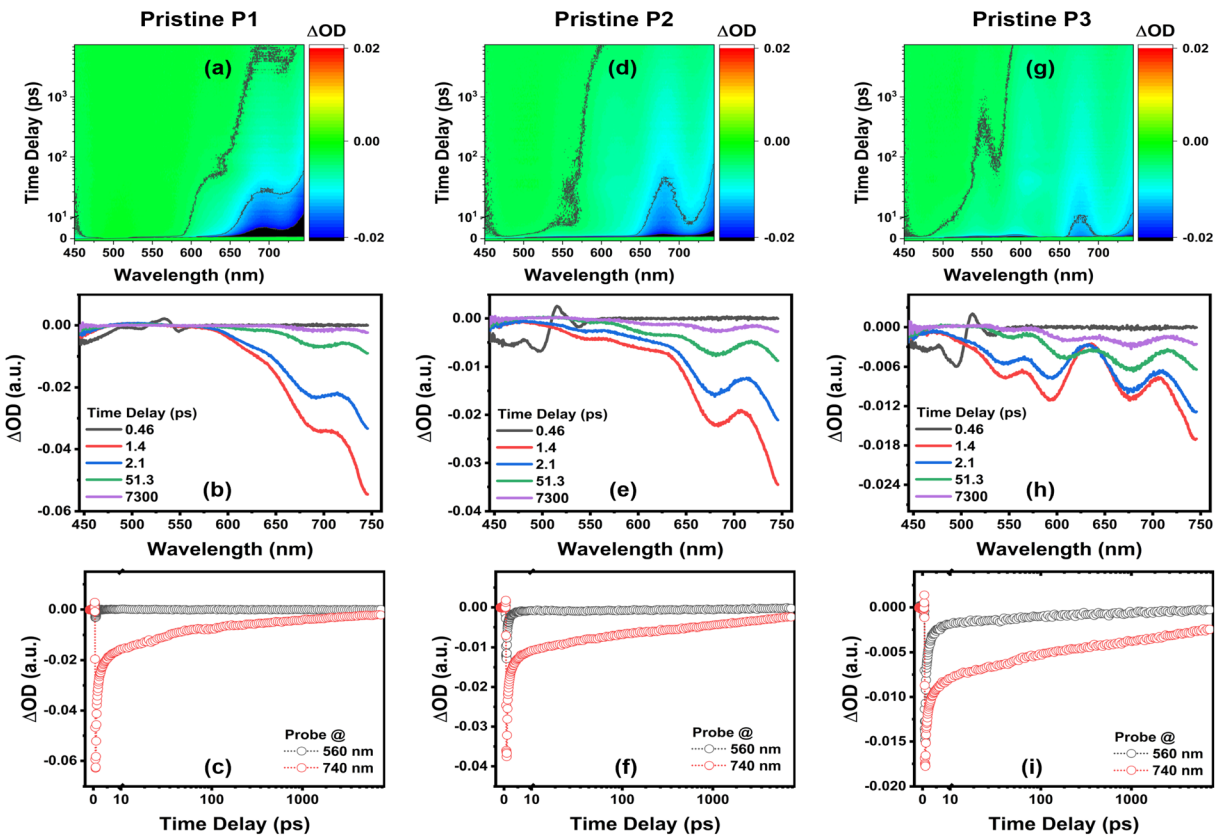

Fig. 3 TA spectra of as-cast pristine (a and b) **P1** (d and e) **P2**, and (g and h) **P3** thin films excited at 800 nm at 1.0 μJ per pulse per cm^2 and probed in the visible region. TA traces probed at different wavelengths from the pristine (c) **P1** (f) **P2** and (i) **P3** films pumped at 800 nm.

molecular dynamics from morphology-driven effects in solid-state films, thus serving as a reference for both pristine terpolymer films and terpolymer : $PC_{71}BM$ blend films. In the case of **P3** in solution, similar to the pristine film, a negative signal is initially observed around 600 nm, followed by a slower negative signal at 740 nm, indicating a sluggish ICT process (around 4.2 ps). Specifically, at early times, the negative signal near 600 nm diminishes over time, while the negative signal near 740 nm and the positive signal at 1030 nm increase. These transient spectral changes provide evidence of the ICT process.[28,29,34–36] Thus, as represented in Fig. 4, high-energy photons excite electrons to the LE state, which then transitions to the ICT state, whereas low-energy excitation directly promotes electrons to the ICT state. The ICT state can be considered a delocalized electronic state within a molecule that facilitates the separation of excitons at the electron donor–acceptor (D/A) interface.

Overall, the comparison of film and solution measurements highlights how molecular composition and morphology jointly dictate ICT formation and recombination dynamics in the pristine terpolymers. While solution studies may capture the intrinsic photophysics of the donor–acceptor backbone, the films reveal additional influences from molecular packing and intermolecular interactions. Fig. 5 and Fig. S7 of the SI display the TA spectra of pristine terpolymer films that have been thermally annealed at 85 °C for 24 h. When connected to the as-cast results, this comparison reveals the impact of morphological evolution induced by thermal stress. Specifically, when compared to the TA data from the as-cast films, the overall TA signal for the GSB of the **P1–P3** terpolymers is markedly diminished after thermal annealing, suggesting reduced exciton generation. While the TA spectra of both the as-cast and annealed pristine terpolymer films exhibit comparable ESA features, the annealed films show a slight spectral blue shift and a slower decay in ESA intensity. Among the three terpolymers, **P1** retains relatively stronger ICT signatures after annealing, consistent with its more robust charge-transfer dynamics, whereas **P2** and especially **P3** show more pronounced loss of ICT intensity and slower decay, reflecting their higher tendency toward exciton recombination.

The thermal annealing results thus highlight how morphological evolution alters exciton generation and recombination and ESA decay, particularly weakening ICT contributions in **P2** and **P3**. To further disentangle the origin of the ESA features and confirm whether they arise from ICT, CS states, or singlet excitons, we extended our analysis to pump fluence–dependent measurements. The ESA band observed in various donor/acceptor alternating copolymers can be attributed to charge-related states, including intramolecular or internal charge transfer (ICT) and charge-separated (CS) states.[37,38] The kinetics of these states typically show a slow rise, significant ESA intensity at extended time delays (greater than 1 ns), and predominantly slow decay during shorter time delays. Fig. S8 of the SI illustrates the evolution of the ESA at 1140 nm for the pristine terpolymers, measured at various pump intensities. The rise of the ESA at 1140 nm occurs within a few hundred femtoseconds following excitation, and the ESA signal nearly disappears after 500 ps. These characteristics differ significantly from those associated with charge-related states, suggesting that the ESA band around 1140 nm primarily corresponds to singlet excitons. At high excitation intensities, singlet exciton–exciton annihilation (EEA) can enhance the recombination of excitons due to a bimolecular reaction.[39–41] However, this effect is minimal in both the as-cast and degraded films, as the decay of the 1140 nm ESA remains consistent across different pump intensities. Consequently, as confirmed by pump fluence-dependent studies (Fig. S8 and S9 of the SI), the decay dynamics of the pristine terpolymer films are largely unaffected by the pump fluence, indicating that the EEA effect is negligible in this investigation.

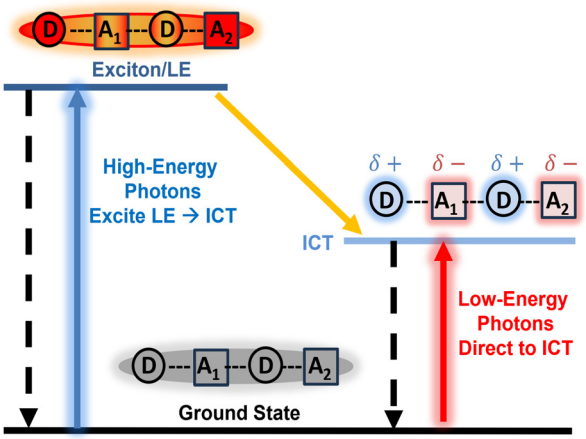

Fig. 4 Dynamics of photoinduced processes in the pristine terpolymers. High-energy excitation promotes electrons to the LE state before relaxation to the ICT state, while low-energy excitation directly populates the ICT state. The ICT state can be considered as a delocalized electronic state that facilitates exciton dissociation at the donor–acceptor interface.

3.3. Transient absorption spectroscopy of terpolymer : $PC_{71}BM$ thin films

The relaxation dynamics of the excited state in terpolymer : $PC_{71}BM$ blend films were examined through TA spectroscopy. Fig. 6 and Fig. S10 and S11 of the SI display the TA spectra of these blend films following the selective excitation of the donor terpolymers at 600 nm. Here, excitons are primarily generated within the donor domains of the BHJ films. In Fig. 6(a and b), the GSB at about 750 nm in the TA spectrum of the **P1** : $PC_{71}BM$ blend film is attributed to the GSB of the **P1** donor terpolymer. In contrast, the TA spectra for the **P2** : $PC_{71}BM$ (Fig. 6(c and d)) and **P3** : $PC_{71}BM$ (Fig. 6(e and f)) blend films show two negative signals near 600 and 750 nm, also corresponding to the donor terpolymer GSB, as seen in Fig. 2 and Fig. S3 of the SI. Each of the three blend films contains positive peaks at approximately 950, 1140, and 1300 nm, with **P1** : $PC_{71}BM$ having an extra ESA peak at around 525 nm. The kinetics of the ESA signal at 1140 nm coincides with that of the GSB signals and is associated with the absorp-

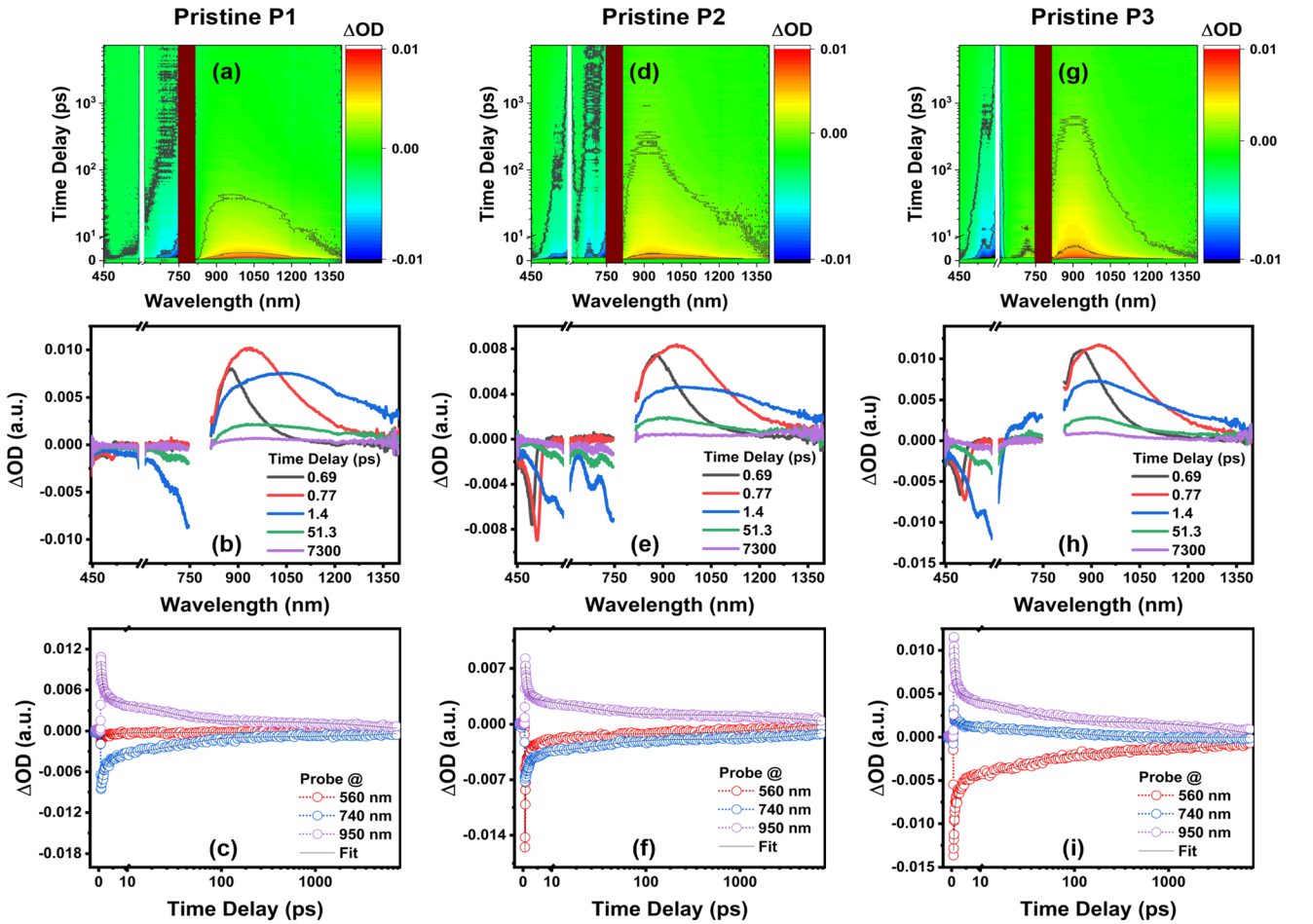

Fig. 5 TA spectra of pristine (a and b) **P1** (d and e) **P2**, and (g and h) **P3** thin films thermally degraded for 24 h and pumped at 600 nm at 1.0 μJ per pulse per cm^2. TA traces probed at different wavelengths from the pristine (c) **P1** (f) **P2** and (i) **P3** films thermally degraded for 24 h and pumped at 600 nm.

tion of either the local excited state or the intermolecular charge transfer state. Additionally, a new peak around 950 nm appears in the near-infrared region of the blended films, likely due to the charge transfer state absorption from the donor to the acceptor. According to the literature, the ESA in **P1** : $PC_{71}BM$, peaking around 525 nm, can be assigned to the absorption of the charge separated state.[42] Furthermore, a new ESA peak emerges at 1300 nm, alongside the GSB of the donor terpolymers, which can be attributed to the ESA signal of the $PC_{71}BM$ acceptor polaron[43] (as illustrated in Fig. S12 of the SI).

These observations under high-energy excitation highlight the presence of both donor- and acceptor-related spectral signatures in the blend films, with distinct ESA contributions that reflect efficient charge generation and separation. To further probe the excitation-wavelength dependence of these dynamics, low-energy photoexcitation was employed. As illustrated in Fig. 7 and Fig. S10 and S13 of the SI, low-energy photons primarily excite the ICT band of the terpolymer : $PC_{71}BM$ blend films. Consequently, the transient spectrum promptly reveals the GSB signal associated with the ICT state, while the GSB signal for the LE state is minimal. Among the three terpolymers, **P1**, which contains the highest proportion of TTDPP, exhibits a more rapid ICT process, whereas **P3**, which has the highest FTAZ ratio, shows a slower ICT process due to its weaker electron-accepting capability. Specifically, a slightly enhanced ESA signal appears at around 525 nm, near the absorption band of $PC_{71}BM$ in the **P1** : $PC_{71}BM$ blend film, resulting from a more efficient electron transfer from the donor terpolymer **P1** to the acceptor $PC_{71}BM$. These results therefore emphasize how terpolymer composition and excitation energy jointly govern ICT dynamics, highlighting distinct mechanistic pathways in pristine *versus* blended films.

Thus, as depicted in Fig. 6, under high-energy photoexcitation, the transition of **P1** to the ICT state occurs more rapidly than for **P2** and **P3**. Compared to the pristine terpolymer films, the GSB and ESA signals in the as-cast terpolymer : $PC_{71}BM$ blend films display a longer-lasting kinetics since the excitons within the active layers separate into electrons and holes in distinct phases, leading to the formation of loosely bound or completely separated species.[44,45] A similar long-lived TA species has been reported in other BHJ films and has been attributed to radical cation or anion

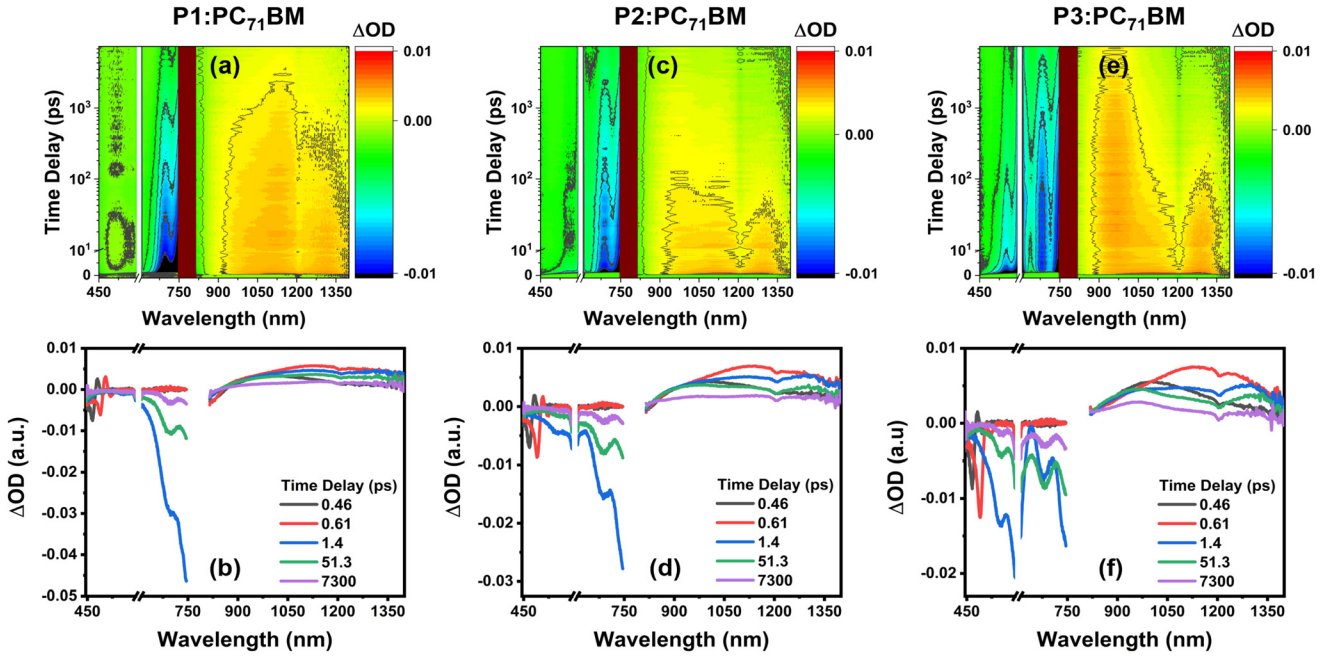

Fig. 6 TA spectra of as-cast (a and b) **P1** : $PC_{71}BM$ (c and d) **P2** : $PC_{71}BM$ and (e and f) **P3** : $PC_{71}BM$ blend films pumped at 600 nm at 0.5 μJ per pulse per cm^2.

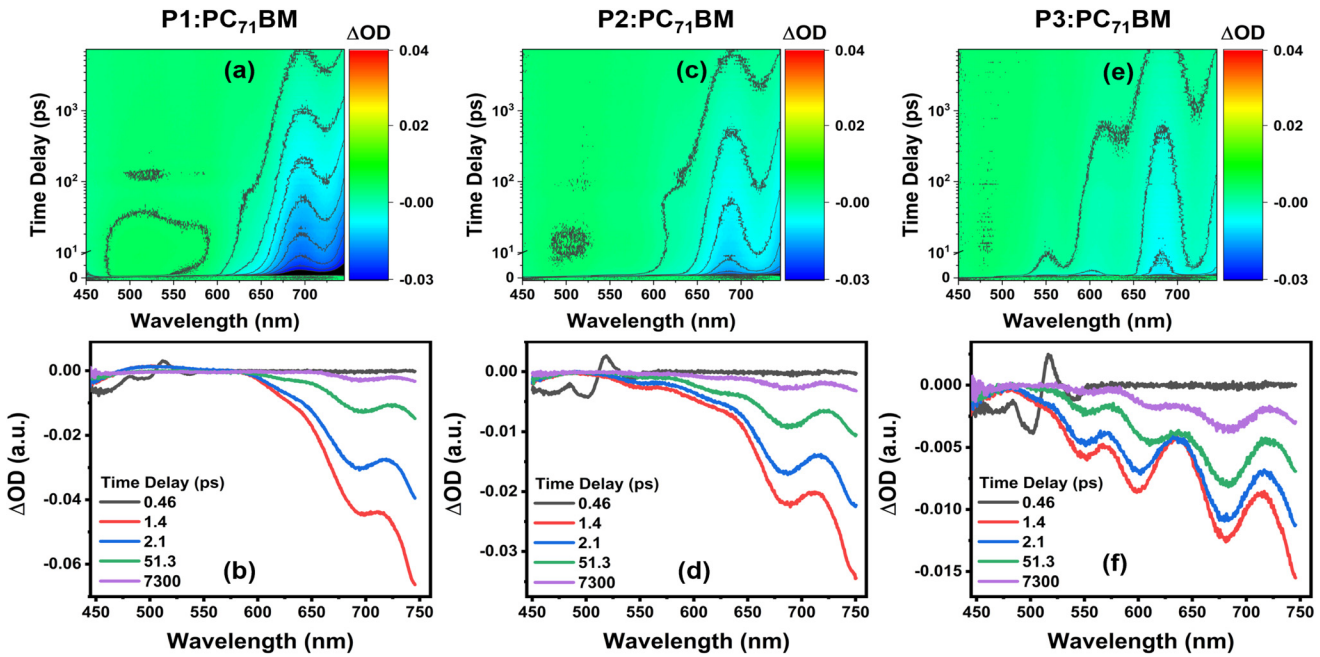

Fig. 7 TA spectra of as-cast (a and b) **P1** : $PC_{71}BM$ (c and d) **P2** : $PC_{71}BM$ and (e and f) **P3** : $PC_{71}BM$ blend films pumped at 800 nm at 1.0 μJ per pulse per cm^2 and probed in the visible region.

species resulting from electrochemical oxidation.[46,47] The presence of the ESA signal around 1300 nm in the blend films further confirms the combination of the two components in the BHJ, as this signal is absent in the TA spectra of the pristine terpolymer films but present in the terpolymer : $PC_{71}BM$ blend films.

These findings confirm that high-energy excitation in the blends not only facilitates faster ICT formation in **P1** compared to **P2** and **P3**, but also promotes the generation of long-lived charge-separated species, as reflected in the extended GSB and ESA dynamics and the emergence of the 1300 nm ESA band. Having established the distinct photophysical be-

havior of the as-cast blends, it is equally important to assess how thermal stress influences these charge dynamics. Thermal annealing is particularly relevant for OSC stability, as it can induce morphology changes that directly affect the recombination of CT states and the efficiency of long-lived charge separation. Accordingly, Fig. 8 and Fig. S10 and S14 of the SI show the TA spectra from terpolymer : $PC_{71}BM$ blend films that underwent thermal annealing for 24 hours at 85 °C. Compared to the as-cast blends, the overall TA signal of the terpolymers' GSB is markedly diminished following thermal annealing, suggesting a reduction in exciton generation, and an increase in the recombination of CT states.

While thermal annealing highlights how morphology changes can influence the recombination of CT states and the lifetime of charge-separated species, it is also crucial to consider how the excitation conditions affect charge dynamics. Specifically, in polymer : fullerene and polymer : polymer blends, high pump fluence levels can trigger bimolecular reactions that increase the decay rate at early times. Within BHJ blends, bimolecular recombination occurs through exciton–exciton annihilation (EEA) and exciton-charge annihilation (ECA), with ECA generally being more significant than EEA. ECA is primarily influenced by the movement of charge carriers, while EEA is reliant on the movement of singlet excitons.[41,48–50] As illustrated in Fig. S15 of the SI, the dynamics of photoinduced absorption at 1140 nm for all BHJ blends show fluence dependence, indicating that bimolecular processes such as non-geminate recombination prevail at high pump fluences. The decay profiles of **P2** : $PC_{71}BM$ and **P3** : $PC_{71}BM$ exhibit a smaller fraction of long-lived separated charge carriers (see Table S2 of the SI), which implies that charge carrier diffusion in these blends is less efficient compared to the **P1** : $PC_{71}BM$ blend film, where diffusion-limited exciton dissociation plays a minor role. At later time intervals, charges become easily identifiable due to the appearance of charge-induced absorption, a behavior that has been documented in other material systems, such as P3HT : PCBM and Si-PCPDTBT : PCBM.[51,52]

Over a timescale of several picoseconds, both as-cast and thermally-annealed terpolymer : $PC_{71}BM$ thin films showed a decrease in the ESA signal intensity at 1140 nm and an increase at 950 nm (see Fig. 6 and 8). We attribute the ESA near 1140 nm to exciton-induced absorption, drawing from its similarity to the ESA observed in the pristine terpolymer films (see Fig. 2), while the ESA at 950 nm is proposed to be linked to charge-induced absorption. This shift suggests that a portion of terpolymer excitons is converted to charge carriers through diffusion-limited exciton dissociation. The assignment of the CT state is further supported by excitation fluence-dependent measurements. The decay dynamics monitored at 950 nm (Fig. S16) and 1140 nm (Fig. S15) exhibit a significant dependence on fluence, indicating bimolecular recombination of free polarons in the CS state. This behavior signifies that charge separation is evident as a second-phase spectral transfer in the terpolymer : $PC_{71}BM$ blend films.

Examining the GSB dynamics of the as-cast and thermally annealed blend samples (Fig. S17), both show significant fluence-independent decay behavior, particularly in the as-cast **P3**-based active layer, suggesting that geminate recombination primarily occurs, reducing the available charge carriers at early times. It's important to note that these bound charges are unlikely to contribute significantly to photocurrent since they do

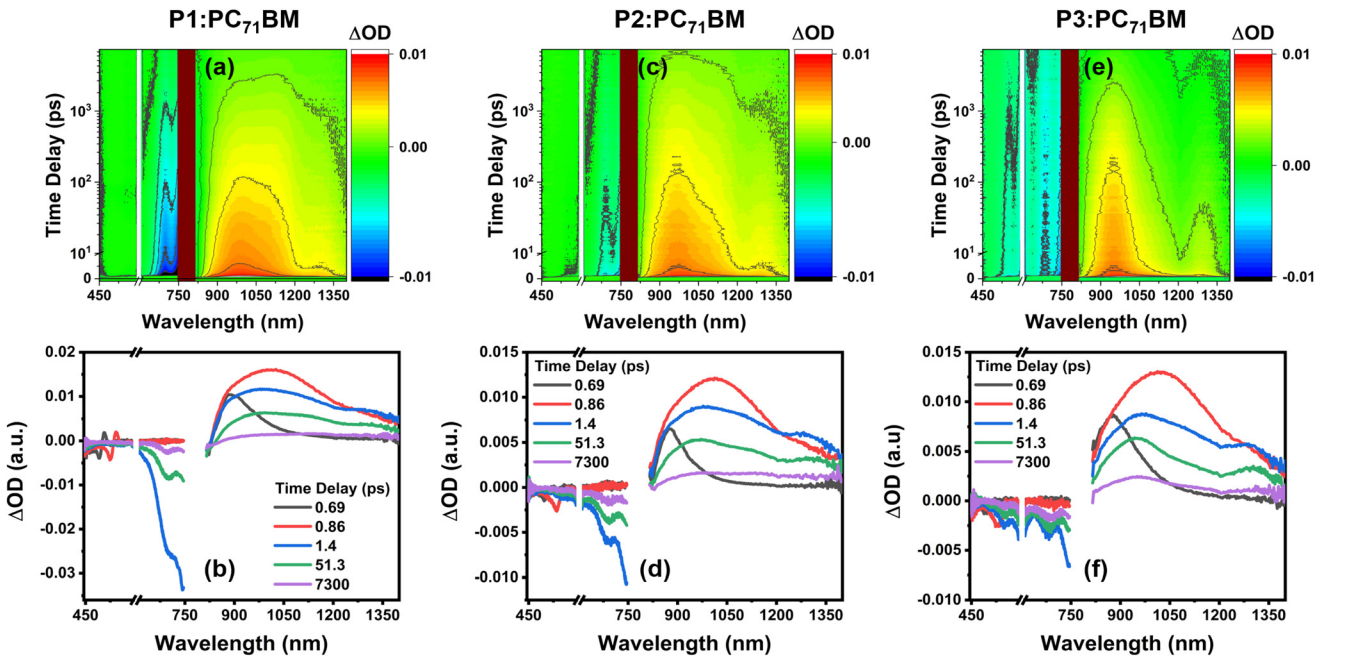

Fig. 8 TA spectra of (a and b) **P1** : $PC_{71}BM$ (c and d) **P2** : $PC_{71}BM$ and (e and f) **P3** : $PC_{71}BM$ blend films thermally degraded for 24 h and pumped at 600 nm at 0.5 μJ per pulse per cm^2.

not fully separate and recombine rapidly. This observation helps explain the lower EQE in **P2** and **P3**-based devices[11] compared to those based on **P1**; the **P2** : $PC_{71}BM$ and **P3** : $PC_{71}BM$ blends likely experience less efficient charge generation and/or greater losses from geminate recombination.

The observed fluence-independent decay and the prevalence of geminate recombination in **P2**- and **P3**-based blends indicate that, despite initial charge generation, many excitons fail to separate efficiently at the electron D/A interface. To further quantify these dynamics and gain insight into exciton diffusion and charge separation efficiencies, we analyzed the ESA around 1140 nm using a multi-exponential fitting approach. The multi-exponential function $I = A_1 e^{\frac{-t}{\tau_1}} + A_2 e^{\frac{-t}{\tau_2}} + A_3 e^{\frac{-t}{\tau_3}}$ was employed to fit the exciton lifetime of the ESA around 1140 nm, where τ_1, τ_2, and τ_3 represent the early-time relaxation of non-equilibrated excitons, the effective exciton lifetime after initial relaxation (which includes diffusion-limited quenching at interfaces before dissociation), and the lifetime of long-lived separated charge carriers, respectively. Fitting the lifetime at 1140 nm alongside other selected wavelength traces (Fig. S18 of the SI) provided time constants along with their corresponding amplitudes as shown in Table S2, which reveal that exciton diffusion in **P2** : $PC_{71}BM$ (τ_2 = 70.71 ps) and **P3** : $PC_{71}BM$ (τ_2 = 92.42 ps) is more efficient than in **P1** : $PC_{71}BM$ (τ_2 = 278.60 ps) BHJs. This indicates that following photoexcitation, excitons in the terpolymer donor form quickly within the donor domains, then migrate promptly to the electron D/A interface. However, slower ICT processes in the **P2** and **P3** terpolymers restrict further exciton diffusion, limiting efficient charge transfer pathways at the interface and leading to recombination at the electron D/A interface. The slow recombination at the CT state in the **P1** : $PC_{71}BM$ active layer could contribute to enhancing the OSC performance, as rapid decay of geminate pairs might hinder the formation of free charge carriers. Moreover, the rise time of the ESA signals in terpolymer : $PC_{71}BM$ films shows a fluence-independent behavior (see Fig. S15 and S16), similar to observations in other BHJ OSC active layers.[45,53] This characteristic suggests that neither ECA nor EEA impacts the formation of the initial CT state.

These results correspond with observations in terpolymer : $PC_{71}BM$-based solar cells, where electron mobility was found to be lower than hole mobility, with **P3**-based active layers displaying the lowest electron mobility (Table S1 of the SI).[11] The rapid sub-10 ps relaxation of hot excitons and substantial proportion of long-lived separated charge carriers correspond with the improved device performance of the **P1** : $PC_{71}BM$-based devices. However, after thermal annealing, all three blend films showed a marked reduction in long-lived separated charge carriers due to fullerene acceptor aggregation, which diminished phase separation. In our previous report,[15] **P1**-based active layers exhibited reduced crystallinity, while **P2**- and **P3**-based active layers showed more stable morphologies after 24 hours of thermal degradation. Generally, reduced crystallinity leads to finer phase mixing, increasing the D/A interfacial area while suppressing large-scale phase separation, suggesting that integrating TTDPP in the terpolymers accelerates exciton dissociation and enhances exciton diffusion to the D/A interface, reducing recombination likelihood and improving FF. This result is supported by the relatively faster exciton diffusion time in the thermally annealed blend films, indicating faster exciton diffusion in the pure terpolymer phases after thermal annealing. However, aggregation of the fullerene acceptor after thermal annealing limits exciton separation at the electron D/A interface. These findings therefore suggest faster electron transfer at **P1** : $PC_{71}BM$ interfaces than at **P2** : $PC_{71}BM$ and **P3** : $PC_{71}BM$ interfaces. Additionally, **P1** : $PC_{71}BM$ blends exhibited smaller domain sizes than **P2** : $PC_{71}BM$ and **P3** : $PC_{71}BM$ blends, even after thermal degradation as evident in the AFM (Fig. S1) and TEM (Fig. S2) analysis reported previously,[15] enabling effective exciton dissociation at D/A interfaces.

Based on the above analysis, the charge carrier kinetics in the BHJ can be simplified as shown in Fig. S19 of the SI. When photons are absorbed, excitons are generated within the terpolymer donor regions in the BHJ films. These photogenerated excitons migrate toward the terpolymer : $PC_{71}BM$ (D/A) interfaces, where they either dissociate into free charge carriers or relax back to their ground state *via* radiative or non-radiative recombination. During exciton separation, the electrons and holes move towards opposite electrode terminals, resulting in photocurrent generation. For the **P1** : $PC_{71}BM$ blend, higher electron mobility enables efficient conversion, leading to an overall higher efficiency. However, for **P2** : $PC_{71}BM$ and **P3** : $PC_{71}BM$, the slower ICT process in the **P2** and **P3** terpolymers reduces electron mobility. This causes charge accumulation near the interface, enhancing recombination losses and thereby lowering the PCE.

4. Conclusions

In summary, we systematically investigated three DPP-based terpolymers, characterized by differences in the ratios of the two acceptors, FTAZ and TTDPP, and their impact on charge carrier dynamics in both pristine terpolymer films and terpolymer : $PC_{71}BM$ blend films. The **P1** terpolymer, with the highest TTDPP content, adopted a more planar molecular backbone, enhancing π–π stacking and non-covalent intermolecular interactions, which together facilitated extended π-conjugation and reduced over-aggregation. These structural features led to a redshifted absorption into the near-infrared region and promoted efficient intramolecular charge transfer, as confirmed by femtosecond transient absorption spectroscopy. The improved π-charge delocalization and balanced carrier mobilities in **P1** translated into superior photovoltaic performance compared to **P2** and **P3**, as reported in our previous publication.[11] Upon light absorption by the active layers, excitons are generated within the terpolymer donor domains of the BHJ films. These excitons diffuse toward the terpolymer : $PC_{71}BM$ donor–acceptor interfaces, where they

either dissociate into free charge carriers or recombine through radiative or non-radiative pathways. Successful exciton dissociation produces electrons and holes that migrate toward opposite electrodes, thereby generating photocurrent. In the **P1** : $PC_{71}BM$ blend, higher electron mobility and more efficient ICT facilitate effective exciton separation and extraction, resulting in superior device efficiency. In contrast, the slower ICT processes in the **P2** and **P3** terpolymers limit electron mobility, increasing the likelihood of exciton accumulation and rapid interfacial recombination. This reduced charge transport efficiency ultimately lowers the PCE in the **P2**- and **P3**-based devices. On the other hand, thermal annealing further reduced the population of long-lived charge carriers in all blends due to fullerene acceptor aggregation, highlighting the delicate interplay between molecular design, nanoscale morphology, and charge transport. Collectively, these results demonstrate that rational tuning of acceptor ratios in DPP-based terpolymers enables precise control over photophysical processes and morphological stability, providing a viable pathway toward optimizing both efficiency and stability in OSCs.

Author contributions

LTN performed the experimental work, data analysis and interpretation, and wrote the manuscript. WM and ZG synthesized the polymers. NAT supervised the research, contributed to the data interpretation, and reviewed and edited the manuscript. DMG provided the experimental resources, contributed to the data interpretation, and reviewed the manuscript. TPJK conceptualized the research, acquired funding, supervised and validated the research, contributed to the data interpretation, and reviewed and edited the manuscript.

Conflicts of interest

There are no conflicts to declare.

Data availability

The data supporting this article have been included as part of the supplementary information (SI). Supplementary information is available. See DOI: https://doi.org/10.1039/d6nr00012f.

Acknowledgements

This work is based on the research supported in part by the National Research Foundation of South Africa Grants No. PMDS22063029254 (LTN) and 120387 and 137973 (TPJK), the African Laser Centre Project No. HLHA23X (LTN), the German Academic Exchange Service (DAAD) Research Grants – Short–Term Grants, 2024 (91897176) (LTN), the Rental Pool Program of the Council for Scientific and Industrial Research's Photonics Centre, South Africa (TPJK), the University of Pretoria (LTN), and the Bavarian initiative "Solar Technologies go Hybrid" (DMG). WM acknowledges financial support from the International Science Programme (ISP), Uppsala University, Sweden.

References

1 L. Lu, T. Zheng, Q. Wu, A. M. Schneider, D. Zhao and L. Yu, *Chem. Rev.*, 2015, **115**, 12666–12731.
2 J. Fu, Q. Yang, P. Huang, S. Chung, K. Cho, Z. Kan, H. Liu, X. Lu, Y. Lang, H. Lai, F. He, P. W. K. Fong, S. Lu, Y. Yang, Z. Xiao and G. Li, *Nat. Commun.*, 2024, **15**, 1830.
3 H. Chen, Y. Huang, R. Zhang, H. Mou, J. Ding, J. Zhou, Z. Wang, H. Li, W. Chen, J. Zhu, Q. Cheng, H. Gu, X. Wu, T. Zhang, Y. Wang, H. Zhu, Z. Xie, F. Gao, Y. Li and Y. Li, *Nat. Mater.*, 2025, **24**, 444–453.
4 H. Ren, J.-D. Chen, Y.-F. Zhang, J.-L. Zhang, W.-S. Chen, Y.-Q. Li and J.-X. Tang, *Sci. Adv.*, 2024, **10**, eadp9439.
5 Y. Sun, L. Wang, C. Guo, J. Xiao, C. Liu, C. Chen, W. Xia, Z. Gan, J. Cheng, J. Zhou, Z. Chen, J. Zhou, D. Liu, T. Wang and W. Li, *J. Am. Chem. Soc.*, 2024, **146**(17), 12011–12019.
6 S. Guan, Y. Li, C. Xu, N. Yin, C. Xu, C. Wang, M. Wang, Y. Xu, Q. Chen, D. Wang, L. Zuo and H. Chen, *Adv. Mater.*, 2024, 2400342.
7 Y. Jiang, S. Sun, R. Xu, F. Liu, X. Miao, G. Ran, K. Liu, Y. Yi, W. Zhang and X. Zhu, *Nat. Energy*, 2024, **9**, 975–986.
8 Z. Zheng, J. Wang, P. Bi, J. Ren, Y. Wang, Y. Yang, X. Liu, S. Zhang and J. Hou, *Joule*, 2022, **6**, 171–184.
9 Y. Wang, J. Luke, A. Privitera, N. Rolland, C. Labanti, G. Londi, V. Lemaur, D. T. W. Toolan, A. J. Sneyd, S. Jeong, D. Qian, Y. Olivier, L. Sorace, J.-S. Kim, D. Beljonne, Z. Li and A. J. Gillett, *Joule*, 2023, **7**, 810–829.
10 G. Li, W.-H. Chang and Y. Yang, *Nat. Rev. Mater.*, 2017, **2**, 17043.
11 A. Negash, Z. Genene, R. T. Eachambadi, J. Kesters, N. V. d. Brande, J. D'Haen, H. Penxten, B. Abdulahi, E. Wang, K. Vandewal, W. Maes, W. Mammo, J. Manca and S. Admassie, *J. Mater. Chem. C*, 2019, **7**, 3375–3384.
12 M. J. Newman, E. M. Speller, J. Barbé, J. Luke, M. Li, Z. Li, Z.-K. Wang, S. M. Jain, J.-S. Kim, H. K. H. Lee and W. C. Tsoi, *Sci. Technol. Adv. Mater.*, 2018, **19**, 194–202.
13 E. M. Speller, A. J. Clarke, N. Aristidou, M. F. Wyatt, L. Francàs, G. Fish, H. Cha, H. K. H. Lee, J. Luke, A. Wadsworth, A. D. Evans, I. McCulloch, J.-S. Kim, S. A. Haque, J. R. Durrant, S. D. Dimitrov, W. C. Tsoi and Z. Li, *ACS Energy Lett.*, 2019, **4**, 846–852.
14 N. Bekri, E. Asmare, W. Mammo and N. A. Tegegne, *Mater. Res. Express*, 2022, **9**, 055502.
15 L. T. Nchinda, Z. Genene, W. Mammo, N. A. Tegegne and T. P. J. Krüger, *New J. Chem.*, 2024, **48**, 10201–10212.
16 N. A. Tegegne, L. T. Nchinda and T. P. J. Krüger, *Adv. Opt. Mater.*, 2024, **13**, 2402257.
17 T. E. Kang, K.-H. Kim and B. J. Kim, *J. Mater. Chem. A*, 2014, **2**, 15252–15267.

18 Z. Li, X. Xu, W. Zhang, X. Meng, W. Ma, A. Yartsev, O. Inganäs, M. R. Andersson, R. A. J. Janssen and E. Wang, *J. Am. Chem. Soc.*, 2016, **138**, 10935–10944.
19 H. Jung, G. Yu, J. Kim, H. Bae, M. Kim, K. Kim, B. Kim and Y. Lee, *Sol. RRL*, 2021, **5**, 2100513.
20 M. Jeong, S. Chen, S. M. Lee, Z. Wang, Y. Yang, Z.-G. Zhang, C. Zhang, M. Xiao, Y. Li and C. Yang, *Adv. Energy Mater.*, 2018, **8**, 1702166.
21 M. Jeong, J. Oh, Y. Cho, B. Lee, S. Jeong, S. M. Lee, S. H. Kang and C. Yang, *Adv. Funct. Mater.*, 2021, **31**, 2102371.
22 P. Tyagi, S.-C. Hua, D. R. Amorim, R. M. Faria, J. Kettle and M. Horie, *Org. Electron.*, 2018, **55**, 146–156.
23 S. Yang, J. Pan, S. Wu, D. Luo, X. Shen, F. Peng and Y. Zhang, *Nanopart. Res.*, 2023, **25**, 134.
24 P. Veerender, V. Saxena, A. K. Chauhan, S. P. Koiry, P. Jha, A. Gusain, S. Choudhury, D. K. Aswal and S. K. Gupta, *Sol. Energy Mater. Sol. Cells*, 2014, **120**, 526–535.
25 P. Cheng and X. Zhan, *Chem. Soc. Rev.*, 2016, **45**, 2544–2582.
26 K. G. Jespersen, W. J. Beeken, Y. Zaushitsyn, A. Yartsev, M. Andersson, T. Pullerits and V. Sundström, *J. Chem. Phys.*, 2004, **121**, 12613–12617.
27 Y. Liu, J. Zhao, Z. Li, C. Mu, W. Ma, H. Hu, K. Jiang, H. Lin, H. Ade and H. Yan, *Nat. Commun.*, 2014, **5**, 5293.
28 S. I. Druzhinin, P. Mayer, D. Stalke, R. von Buelow, M. Noltemeyer and K. A. Zachariasse, *J. Am. Chem. Soc.*, 2010, **132**, 7730–7744.
29 R. Ghosh and D. K. Palit, *J. Phys. Chem. A*, 2012, **116**, 1993–2005.
30 H. Lu, X. Wang, H. Wang, A. Zhang, X. Zheng, N. Yu, Z. Tang, X. Xu, Y. Liu, Y.-N. Chen and Z. Bo, *Sci. China: Chem.*, 2022, **65**, 594–601.
31 S. Holliday, R. S. Ashraf, A. Wadsworth, D. Baran, S. A. Yousaf, C. B. Nielsen, C.-H. Tan, S. D. Dimitrov, Z. Shang, N. Gasparini, M. Alamoudi, F. Laquai, C. J. Brabec, A. Salleo, J. R. Durrant and I. McCulloch, *Nat. Commun.*, 2016, **7**, 11585.
32 J. Hai, W. Zhao, S. Luo, H. Yu, H. Chen, Z. Lu, L. Li, Y. Zou and H. Yan, *Dyes Pigm.*, 2021, **188**, 109171.
33 G. Zhang, X.-K. Chen, J. Xiao, P. C. Y. Chow, M. Ren, G. Kupgan, X. Jiao, C. C. S. Chan, X. Du, R. Xia, Z. Chen, J. Yuan, Y. Zhang, S. Zhang, Y. Liu, Y. Zou, H. Yan, K. S. Wong, V. Coropceanu, N. Li, C. J. Brabec, J.-L. Bredas, H.-L. Yip and Y. Cao, *Nat. Commun.*, 2020, **11**, 3943.
34 R. Ghosh, A. Nandi and D. K. Palit, *Phys. Chem. Chem. Phys.*, 2016, **18**, 7661–7671.
35 S. I. Druzhinin, V. A. Galievsky, A. Demeter, S. A. Kovalenko, T. Senyushkina, S. R. Dubbaka, P. Knochel, P. Mayer, C. Grosse, D. Stalke and K. A. Zachariasse, *J. Phys. Chem. A*, 2015, **119**, 11820–11836.
36 M. A. Kochman and B. Durbeej, *J. Phys. Chem. A*, 2020, **124**, 2193–2206.
37 D. Peckus, A. Devižis, D. Hertel, K. Meerholz and V. Gulbinas, *Chem. Phys.*, 2012, **42**, 404.
38 B. S. Rolczynski, J. M. Szarko, H. J. Son, Y. Liang, L. Yu and L. X. Chen, *J. Am. Chem. Soc.*, 2012, **134**, 4142–4152.
39 J. Guo, H. Ohkita, H. Benten and S. Ito, *J. Am. Chem. Soc.*, 2009, **131**, 16869–16880.
40 I. B. Martini, A. D. Smith and B. J. Schwartz, *Phys. Rev. B: Condens. Matter Mater. Phys.*, 2004, **69**, 035204.
41 A. A. Paraecattil, S. Beaupré, M. Leclerc, J.-E. Moser and N. Banerji, *J. Phys. Chem. Lett.*, 2012, **3**, 2952–2958.
42 R. Wang, C. Zhang, Q. Li, Z. Zhang, X. Wang and M. Xiao, *J. Am. Chem. Soc.*, 2020, **142**, 12751–12759.
43 M. Liedtke, A. Sperlich, H. Kraus, C. Deibel, V. Dyakonov, S. Filippone, J. L. Delgado, N. Martín and O. G. Poluektov, *ECS Trans.*, 2010, **28**, 3.
44 M. Tong, N. E. Coates, D. Moses, A. J. Heeger, S. Beaupré and M. Leclerc, *Phys. Rev. B: Condens. Matter Mater. Phys.*, 2010, **81**, 125210.
45 I.-S. Kim, S.-Y. Jang, T. Park, C. Jo, D.-Y. Kim and D.-K. Ko, *Chem. Phys.*, 2015, **461**, 29–33.
46 J. Guo, Y. Liang, J. Szarko, B. Lee, H. J. Son, B. S. Rolczynski, L. Yu and L. X. Chen, *J. Phys. Chem. B*, 2010, **114**, 742–748.
47 K. Yonezawa, H. Kamioka, T. Yasuda, L. Han and Y. Moritomo, *Appl. Phys. Express*, 2012, **5**, 042302.
48 J. M. Hodgkiss, S. Albert-Seifried, A. Rao, A. J. Barker, A. R. Campbell, R. A. Marsh and R. H. Friend, *Adv. Funct. Mater.*, 2012, **22**, 1567.
49 A. J. Ferguson, N. Kopidakis, S. E. Shaheen and G. Rumbles, *J. Phys. Chem. C*, 2008, **112**, 9865–9871.
50 I. A. Howard, J. M. Hodgkiss, X. Zhang, K. R. Kirov, H. A. Bronstein, C. K. Williams, R. H. Friend, S. Westenhoff and N. C. Greenham, *J. Am. Chem. Soc.*, 2010, **132**, 328–335.
51 F. Etzold, I. A. Howard, N. Forler, A. Melnyk, D. Andrienko, M. R. Hansen and F. Laquai, *Energy Environ. Sci.*, 2015, **8**, 1511–1522.
52 S. Karuthedath, T. Sauermann, H.-J. Egelhaaf, R. Wannemacher, C. J. Brabec and L. Lüer, *J. Mater. Chem. A*, 2015, **3**, 3399–3408.
53 I.-S. Kim, S. Kwon, J. Kim, D.-Y. Kim and D.-K. Ko, *Polymer*, 2015, **63**, 208.